Nondestructive three-dimensional element-concentration mapping of a Cs-doped partially molten granite by X-ray computed tomography using synchrotron radiation

Susumu Ikeda,[1,*] Tsukasa Nakano,[2] Akira Tsuchiyama,[3] Kentaro Uesugi,[4] Yoshio Suzuki,[4] Ko-ichi Nakamura,[2] Yoshito Nakashima,[2] and Hideto Yoshida[5]

[1]Department of Complexity Science and Engineering, Graduate School of Frontier Sciences, The University of Tokyo, Kashiwanoha 5-1-5, Kashiwa, Chiba 277-8561, Japan
[2]National Institute of Advanced Industrial Science and Technology (AIST), Tsukuba, Ibaraki 305-8567, Japan
[3]Department of Earth and Space Science, Graduate School of Science, Osaka University, Toyonaka, Osaka 560-0043, Japan
[4]Japan Synchrotron Radiation Research Institute (JASRI/SPring-8), Mikazuki, Hyogo 679-5198, Japan
[5]Department of Earth and Planetary Science, Graduate School of Science, The University of Tokyo, Bunkyo-ku, Tokyo 113-0033, Japan

ABSTRACT

Nondestructive, three-dimensional (3-D) element-concentration mapping was performed and high spatial resolution and quantitative applicability were demonstrated. X-ray computed tomography using synchrotron radiation developed at SPring-8 (SP-μCT) enabled us to acquire high-resolution tomographic images with X-ray energies just above and below the absorption edge of an element. Concentration of the element could be calculated from the difference of these images with a correction using standard material. A 3-D Cs concentration map of a partially molten granite was obtained by this technique and compared with a 2-D element map produced by an electron-probe X-ray microanalyzer (EPMA), with respect to spatial and compositional resolution. A spatial resolution of about 20 μm was achieved by SP-μCT. The compositional resolution of ±2.5 wt% was achieved using the following two calibration processes of linear attenuation coefficients (LAC): (1) calibration based on the empirical relationship between theoretical LACs and observed CT values, and (2) the calibration of spatial variation of observed mass attenuation coefficients (MAC) due to X-ray energy shift using a standard material (Cs-bearing solution). Using the Cs_2O map obtained by SP-μCT, 3-D image analysis was demonstrated, for example, connectivity of melt was calculated and it was found that 88 vol% of melt was connected in three dimensions in the sample. Furthermore, the possibility of 3-D diffusion studies by SP-μCT was discussed based on the spatial and compositional resolutions. This "nondestructive" and "3-D" mapping technique can reveal the internal compositional distribution of precious samples such as extraterrestrial materials and cultural assets, and can solve many 3-D issues such as material transport in geological and industrial materials.

INTRODUCTION

X-ray computed tomography (CT) is a nondestructive technique for obtaining the spatial distribution of the X-ray linear attenuation coefficient (LAC; denoted by μ) in an object. The synchrotron radiation (SR) source provides highly collimated (parallel) and monochromatized X-ray beams useful for X-ray CT (Flannery et al. 1987; Bonse and Busch 1996), and is beginning to be used for mineralogical and petrological X-ray CT studies (e.g., Uesugi et al. 1999; Tsuchiyama et al. 2001; Paktunc et al. 2001). Collimated X-ray beams allow us to obtain high-spatial-resolution X-ray CT images straightforward without data corrections required when using fan beams or cone beams (Herman 1980; Kak and Slaney 1988). The monochromatic X-ray beams enable the calculation of quantitative values of the LAC that depend on only the chemical composition and density of a material. Moreover, we can map the element concentration in an object using the X-ray CT images measured at the tuned photon energies. Using X-ray CT with an SR source, Thompson et al. (1984) obtained a two-dimensional (2-D) map of I. The map consisted of a differential image of two X-ray CT images measured

at photon energies just above and below the *K*-absorption edge of I. The technique, generally called the "subtraction method," is based on the nature of X-ray absorption, whereby the changes in the LACs of other elements are negligible within a small energy range around the absorption edge. In later studies, the subtraction method was applied to the imaging of Ni (Kinney et al. 1986), Cu (Flannery et al. 1987; Kinney et al. 1986), and Mo (Suzuki et al. 1988). In those studies, only qualitative images were obtained, and no quantitative discussion of the concentration was involved. The first demonstration that the internal element concentration could be quantified by the subtraction method was performed by Hirano et al. (1989). They acquired two CT images (below and above Mo K-edge) of a set of several tubes containing Mo solution with different concentrations. They obtained a differential image by subtraction and estimated the Mo concentrations using the average CT value in each solution. They did not discuss the spatial resolution as a concentration map (whether each pixel had quantitative meaning), though they mentioned that the spatial resolution of their CT system was about 125 μm. In this paper, we report three-dimensional (3-D) concentration mapping obtained by the high-spatial-resolution X-ray CT system developed at SPring-8 (Super Photon ring-8 GeV, Hyogo, Japan). Further-

---

more, we discuss the quantitative applicability of the mapping technique by comparison with a 2-D element map measured by an electron-probe X-ray microanalyzer (EPMA).

X-RAY CT SYSTEM OF SPRING-8 (SP-μCT)

In recent years, an X-ray CT system named "SP-μCT" with high spatial and contrast resolution, using SR, has been developed at beam line BL20B2 of SPring-8 (e.g., Uesugi et al. 1999; Tsuchiyama et al. 1999). BL20B2 is a bending-magnet beam line with a Si (311) double-crystal monochromator at 45 m from the light source, producing monochromatic X-rays with a flux density of $\sim 1 \times 10^9$ photons/s·mm². The usable energy range is 8.4–72 keV (Uesugi et al. 1999; Goto et al. 2001). The transmitted X-rays are converted to visible light by a fluorescent screen of Tb-doped Gd_2O_2S, expanded by an optical lens (magnification ×2), and detected by a CCD camera with the pixels of 1000 × 1018 (Uesugi et al. 1999; Takano et al. 2001). After the ordinary pre-processing for raw X-ray intensities and their logarithm conversion, a convolution back-projection (CBP) method with a reconstruction filter using a Hanning-window is used to reconstruct the CT images from the projection data (Uesugi et al. 1999; Nakano et al. 2000). Each CT image (1000 × 1000 pixels as the maximum) has a pixel size of 5.83×5.83 μm² and a thickness of 5.83 μm. The effective spatial resolution of the SP-μCT is about 13 μm, according to the results of imaging tests with X-ray energies less than 20 keV (Uesugi et al. 1999; Takano et al. 2001). The spatial resolution of the image detector was slightly greater than 13 μm at the energy of 36 keV used in this study because of blur of the X-ray in the thin fluorescent screen. The contrast resolution of the system was reported by Uesugi et al. (1999). The diameter (maximum width) of samples must be less than 5 mm, as it is restricted by the field of view of the detector. A sample height up to several centimeters is permitted, although actual imaging area is less than 5 mm in height owing to the divergent angle of X-ray beams. Imaging of samples up to several centimeters is possible by connecting several data sets with vertical translations.

EXPERIMENTAL METHODS

Sample synthesis

A Cs-doped, partially molten sample was prepared using natural granite. The Cs was expected to become concentrated in the melt and this would be useful for imaging partial melt and for studying element diffusion in the melt. Fine-grained biotite granite (adamellite having an aplite-like texture) from Hirukawa, Gifu-Prefecture, Japan, was used for sample preparation. Modal composition of the specimen was K-feldspar 34%, plagioclase 31%, quartz 31%, and biotite 4%. The cylindrically formed granite (3 mm in diameter and 10 mm in length) was put into a platinum tube with Cs_2CO_3 powder reagent (2.1 wt% Cs_2O) and pure water (10 wt%; supersaturated amount). First, the specimen was held isothermally at 1000 °C and at an isostatic pressure of 228 MPa with Ar gas in an HIP (Hot Isostatic Press produced by Kobe Steel, Ltd.). This condition (1000 °C) was meant to completely melt the granite specimen in 50 h according to preliminary experiments. After holding for 16 h, when the melt fraction had reached about 10 vol% (based on the preliminary experiments), the temperature was dropped to 800 °C in 2 h. The pressure decreased to 204 MPa with this drop in temperature. After holding at 800 °C for 75 h, the specimen was quenched at room temperature under high-pressure conditions. The volume fraction of the melt was about 10%. If the preheating at 1000 °C is not performed at the first stage, the natural granite specimen (not powder) does not begin melting, and the melt fraction cannot reach 10 vol% within several days. After removal from the platinum tube, the specimen was used for the X-ray CT experiments.

X-ray CT experimental procedure

The cylindrical specimen (3.5 mm in diameter and 6 mm in height) was placed on the rotation stage of the SP-μCT system so that the main axis of the sample became almost the same as the rotation axis of the stage. The system settings were the same as those reported by Uesugi et al. (1999). We obtained two sets of CT images for this sample. One set was obtained at an X-ray energy of 35.970 keV, which is just below the Cs K-absorption edge (35.985 keV) (Hubbell and Seltzer 1996). Another set was obtained at an X-ray energy of 36.000 keV, which is just above the K-absorption edge. To obtain the CT images, 360 transmitted X-ray images (I images) were acquired with a rotation step angle of 0.5 degrees, and exposure time of 35 seconds per rotation step. One image by a direct beam without the sample (I_0 image) was acquired for every ten rotation steps by lowering the sample stage to correct time drift of the X-ray beam intensity. Dark images were also obtained before and after the experiment to eliminate the base intensity without the X-ray beam. A total of 784 tomographic images (2-D slices) were then reconstructed from the 360 projection images. Note that the projection images consist of "projections" as pixel values. The X-ray projection of every pixel, p, is defined by:

$$p = \ln\left(\frac{I_0}{I}\right) = \sum_j \mu_j \, L_j \tag{1}$$

where I_0 and I are the intensities of incident and transmitted X-ray beams, respectively. Projections in each projection image were calculated using the intensities I and I_0 of corresponding pixels in I and I_0 images. The projection p equals to the sum of the LAC of material j (μ_j) multiplied by the path length through material j (L_j).

Tsuchiyama et al. (2000; in preparation) obtained an empirical relationship between the CT value (observed LAC by SP-μCT) and the theoretical LAC for standard materials in the present CT system at the beam line BL20B2. CT-value, f, is almost proportional to LAC, μ, for small μ ($\mu < \sim 20$ cm⁻¹) but deviates from the linear relation for large μ ($\mu > \sim 20$ cm⁻¹). This nonlinear relation can be expressed by the following empirical formula (Tsuchiyama et al. in preparation):

$$\mu = \left[\left(af \right)^n + \left(bf^c \right)^n \right]^{1/n} \tag{2}$$

where the parameter of a, b, c and n were determined by least-squares fitting ($a = 1.127 \pm 0.005$, $b = 0.5819 \pm 0.1414$, $c = 1.227 \pm 0.062$ and $n = 19.4$). In this study, the obtained CT value was converted to the LAC value for each voxel using Equation 2.

Furthermore, we performed another experiment for data correction. We obtained projection images of a quartz glass cell filled with a $CsCO_3$ aqueous solution (Cs = 2.95 wt%) at X-ray energies of 35.970 keV and 36.000 keV. This quartz glass cell has a rectangular shape (outer dimensions: $12.7 \times 12.5 \times 45.0$ mm³; inner dimensions: $10.0 \times 10.1 \times 43.7$ mm³) and is usually used for ultraviolet - visible - near infrared spectrophotometers. First, the net projection of the solution was calculated using the gross projection of the cell and solution and their parameters (chemical composition of the cell: SiO_2, density of the cell = 2.08 g/cm³, and thickness of cell walls that X-rays pass through = 1.35 mm × 2 = 2.70 mm). Second, the difference in the mass-attenuation coefficient (MAC; denoted by τ) above and below the absorption edge was calculated for every pixel using the chemical composition, density, and path length of the solution (10.00 mm). Here, the relationship between MACs, τ, and LACs, μ, is represented by μ (cm⁻¹) = τ (cm²/g) × ρ (g/cm³), where ρ is the density. This measurement of MACs above and below the absorption edge is indispensable to obtain accurate data by the "subtraction method." As discussed later in detail, the difference in MAC ($\Delta\tau_{Cs}$) had variation perpendicular to the ground (the plane of the storage ring). This vertical shift of $\Delta\tau_{Cs}$ results from the shift of X-ray energy which is caused by the variation of the reflection position and angle of the X-ray beam in the double-crystal monochromator with vertical dispersion geometry. The shift value depends on the geometry of the light source, the monochromator, and the sample.

EPMA analysis

To evaluate the spatial and compositional resolution of the present 3-D concentration mapping by SP-μCT, conventional 2-D mapping by an electron-probe X-ray microanalyzer (EPMA) was performed after the X-ray CT experiment. The specimen was mounted in epoxy, ground, and polished. The surface obtained after polishing corresponded to slice no. 252 of the CT images. A JEOL 8900 EPMA at the University of Tokyo was used for this 2-D precise mapping of the surface. The acceleration voltage and beam current used were 15 keV and 1.2×10^{-7} A, respectively. The beam diameter was set at 3 μm. The mapping step was set at 6 μm, similar to the size of one voxel in the CT images. The intensity of the CsL X-rays was

used to determine the concentration at each mapping point. We confirmed the linear relationship between wt% Cs and the intensity of the CsL X-rays by conventional point analysis, at many points in the sample, using ZAF correction. Pure CsI was used as the standard sample to quantify the Cs concentration.

RESULTS AND DISCUSSION

LAC images and estimation of Cs-concentration

Figure 1a shows the CT image of slice no. 252, indicating the 2-D distribution of the LAC converted from CT values. Figure 1b shows the distribution of phases obtained by EPMA element maps. By comparing the two figures, it is clear that the constituent minerals have different LACs and different gray levels in Figure 1a, except for K-feldspar and plagioclase.

Pollucite ($Cs_2Al_2Si_4O_{12} \cdot nH_2O$) was crystallized in a Cs-bearing melt, especially at the periphery of the sample. Table 1 shows the chemical composition, density (Deer et al. 1966; Dana and Ford 1959; Roberts et al. 1974; density of melt was estimated as described later), and calculated attenuation coefficients of minerals and melt. Based on the LACs in the table, K-feldspar and plagioclase have similar LACs and it is theoretically difficult to distinguish them. The ring artifact, one of the typical artifacts in X-ray CT images, is seen to some extent. However, beam hardening, an unavoidable CT artifact when using polychromatic X-rays (Denison et al. 1997; Ketcham and Carlson 2001), does not occur because of the use of monochromatic X-rays. If beam hardening occurs, apparent LAC becomes smaller as it goes to the central part of the sample, and many problems result when
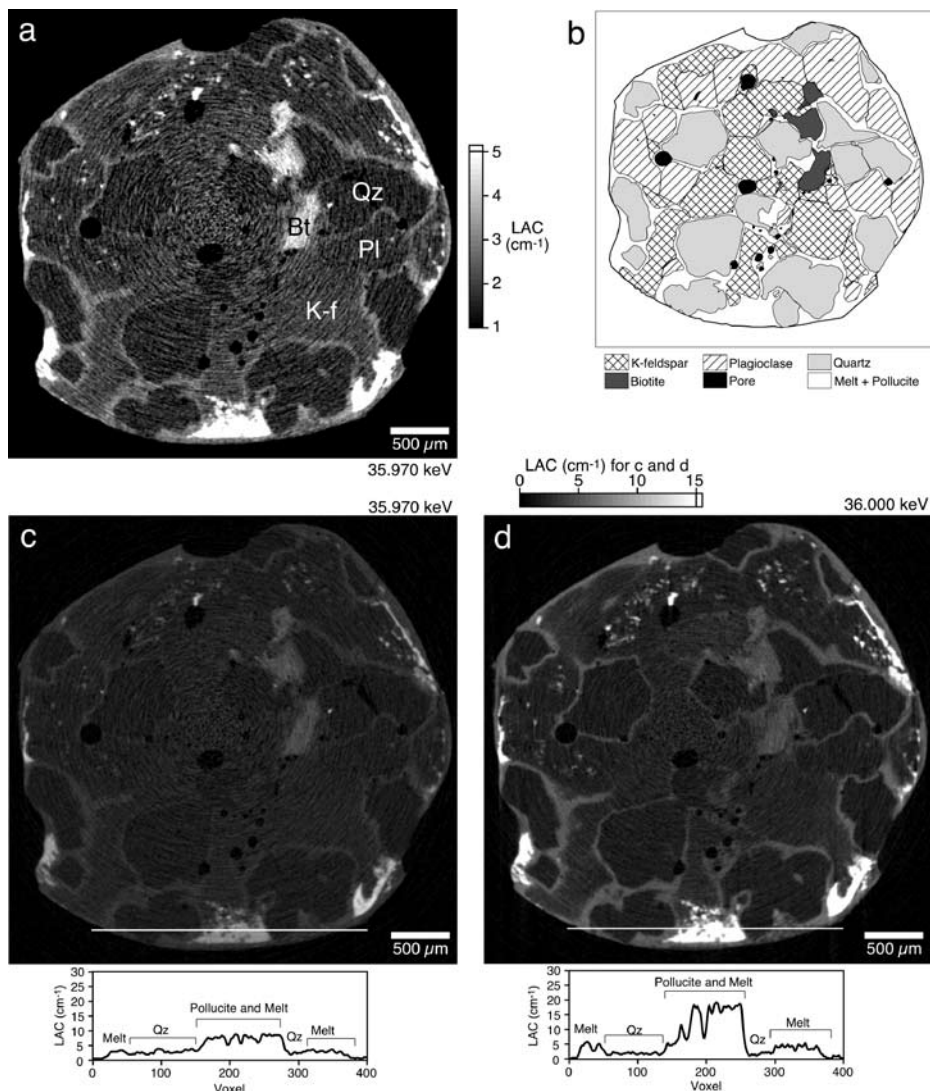

FIGURE 1. (a) One slice from CT images with the X-ray energy just below the Cs K-absorption edge of 35.970 keV (slice no. 252; 650×650 voxels). Gray level corresponds to LAC (1–5 cm^{-1}) calculated from CT values by Equation 2 (in text) as indicated by the gray-scale bar. Theoretical LACs (μ) of all phases are shown in Table 1. Mineral names are as follows: K-f = K-feldspar, Pl = plagioclase, Qz = quartz, Bt = biotite. (b) 2-D distribution of mineral and melt phases determined based on the EPMA element maps of Si, Ti, Al, Fe, Ca, Na, K, and Cs. This polished plane corresponds to slice no. 252 of the CT images. CT images c and d are of slice no. 252 at two X-ray energies just below (35.970 keV) and just above (36.000 keV) the Cs K-absorption edge, respectively, with gray scale 0–15 cm^{-1}. Graphs under the images indicate variation of LAC along the lines shown in the images. Note that a and c are the same image with different gray scales for LACs.

TABLE 1. Typical chemical composition (wt%), density and calculated attenuation coefficients of minerals and melt in the sample

	Quartz	K-feldspar	Plagioclase	Biotite	Pollucite	Melt
			Chemical composition			
SiO_2	99.1	64.4	58.2	32.3	43.8	72.0
TiO_2	0.0	0.0	0.1	3.3	0.0	0.0
Al_2O_3	0.0	19.2	24.6	18.9	17.3	11.7
Fe_2O_3	0.1	0.0	0.2	23.1	0.2	0.1
MnO	0.1	0.0	0.1	0.4	0.0	0.0
MgO	0.0	0.1	0.0	7.3	0.0	0.1
CaO	0.0	0.0	5.4	0.0	0.1	0.3
Na_2O	0.0	2.3	10.0	1.0	1.9	0.7
K_2O	0.0	13.5	0.3	9.2	1.7	2.7
Cs_2O	0.0	0.0	0.2	0.2	33.7	4.8
H_2O*	–	–	–	4.3	1.3	7.6
Total	99.3	99.5	99.1	100.0	100.0	100.0
			Theoretical MAC (cm²/g) at measured X-ray energies			
36.000 keV (above K-edge)	0.57	0.72	0.69	1.44	9.73	1.98
35.970 keV (below K-edge)	0.57	0.72	0.64	1.40	2.15	0.83
Density (g/cm³)	2.65†	2.56†	2.66‡	3.0†	2.9§	2.4‖
			Theoretical LAC (cm⁻¹) at measured X-ray energies			
36.000 keV (above K-edge)	1.51	1.85	1.83	4.32	28.2	4.75
35.970 keV (below K-edge)	1.50	1.84	1.71	4.20	6.24	1.98

* For phases including water, H_2O content was estimated by subtraction of total wt% from 100.
† Deer et al. (1966).
‡ Density of plagioclase depends on Ab-An ratio (Deer et al. 1966) and the value in the table was estimated using the measured Ab-An ratio ($Ab_{77}An_{23}$).
§ e.g., Dana and Ford (1959); Roberts et al. (1974).
‖ Estimated from chemical composition (see text).

quantitative analyses are carried out.

Figures 1c and 1d show CT images with two X-ray energies just above and below the Cs K-absorption edge, respectively. Because of the very small difference in X-ray energy between the two conditions (0.030 keV), there is little difference in the LAC between the two images in the Cs-free regions. For example, quartz grains that contain no Cs show the same gray level in the two images. In contrast, considerable difference occurs in Cs-bearing regions. These regions consist of pollucite crystals and melt containing dissolved Cs. Such a difference in the LAC is induced by the large difference in the MACs of Cs above and below the absorption edge. The MAC for Cs just above the K-absorption edge is about 5 times greater than that just below the edge (Hubbell and Seltzer 1996). As described above, LACs (μ) have the relationship with MACs (τ) represented by μ (cm⁻¹) = τ (cm²/g) $\times \rho$ (g/cm³). We can derive the weight fraction of Cs using the difference in the LAC ($\Delta\mu$) between Figures 1c and 1d as follows. The difference in LAC of each pixel above and below the absorption edge is:

$$\Delta\mu = (\Delta\tau_{Cs}\,\alpha_{Cs} + \textstyle\sum_i \Delta\tau_i\,\alpha_i)\rho \qquad (3)$$

where α_{Cs} is the weight fraction of Cs, $\Delta\tau_{Cs}$ is the difference in the MAC of Cs above and below the Cs K-absorption edge, and i denotes all other elements (modified from Hirano et al. 1989). Because $\Delta\tau_i$ is very small, the second term is negligible compared to the first term, and we obtain the following equation (Hirano et al. 1989):

$$\alpha_{Cs} = \frac{\Delta\mu}{\Delta\tau_{Cs}\,\rho}. \qquad (4)$$

Although the X-rays used in the present study were monochromatic, a small degree of vertical variation of the X-ray energy, which caused changes in $\Delta\tau_{Cs}$, was inevitable in a large beam area (Fig. 2d). The theoretical energy spread in the vertical
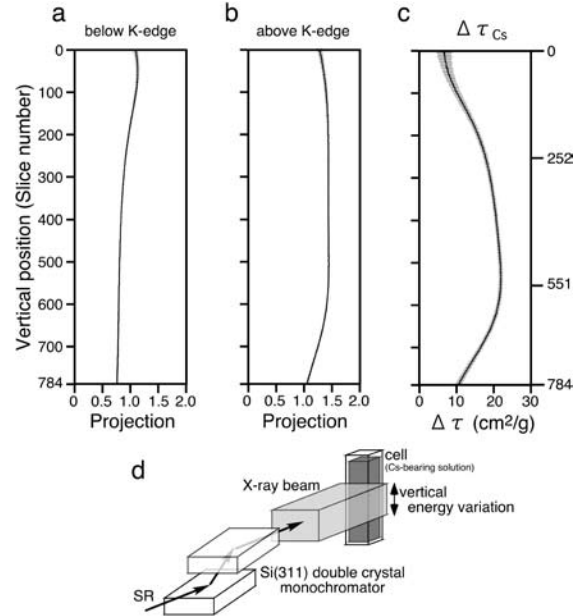

FIGURE 2. Variation in the X-ray projection (line integral of LAC along the X-ray path) through the quartz glass cell filled with Cs-bearing solution measured at X-ray energies of (a) 35.970 keV and (b) 36.000 keV. The sample was not rotated. Variation in the projection indicates the energy shift in the actual X-ray beam. The energy shift is probably due to the X-ray monochromater system shown schematically as d. Using the projection data, path length through the cell, and chemical composition and densities of the solution and the cell, $\Delta\tau_{Cs}$ (the difference in the MAC of Cs above and below the Cs K-edge) of every slice was obtained as c. The projection and $\Delta\tau_{Cs}$ have vertical and horizontal variation. Solid curves indicate mean value in each slice. The horizontal variation (standard deviation) in each slice is shown with gray bar. The horizontal variation of projection and $\Delta\tau_{Cs}$ is negligibly small compared with the vertical one, excepting the top and bottom regions of the X-ray beam.

direction (4 mm) is 0.019 keV assuming that the monochromator is perfect. As described above, the actual vertical distribution of $\Delta\tau_{Cs}$ was measured by acquiring the X-ray projection image of a quartz glass cell filled with a Cs-bearing solution of known concentration. Figures 2a and 2b show actual variations in the X-ray projections through the cell with the X-ray energy just above and below the Cs K-absorption edge, respectively. Figure 2c shows the variation of $\Delta\tau_{Cs}$ obtained using the projection data. The horizontal deviation of $\Delta\tau_{Cs}$ was negligibly small compared with the vertical one as shown by the (horizontal) error bars. To improve the quantitative accuracy of α_{Cs}, we used the measured $\Delta\tau_{Cs}$ in Equation 4 for each slice (i.e. a $\Delta\tau_{Cs}$ value for each slice). Because $\Delta\mu$ can be obtained from the CT images by using Equation 2, the only unknown parameter was ρ. We assumed ρ to be 2.4 g/cm^3 and 2.9 g/cm^3 for the melt and pollucite, respectively. The density of 2.4 g/cm^3 is that of the melt, including 5 wt% Cs$_2$O, estimated by the method proposed by Bottinga et al. (1982). The influences of pressure (about 0.05 g/cm^3 increase at 200 MPa) and water content (about 0.05 g/cm^3 decrease at 5 wt% H$_2$O) (Johannes and Holtz 1996) were also taken into consideration. According to the EPMA measurements, the solubility of Cs to the partial melt in the specimen was less than 6 wt% as Cs$_2$O. The mapping points which had Cs$_2$O concentrations greater than 6 wt% included the contribution from pollucite. The estimated melt density of 2.4 g/cm^3 could be applicable to the regions with Cs$_2$O concentrations less than 6 wt%.

Cs-concentration maps and their resolutions

Figures 3a and 3b show Cs$_2$O concentration maps obtained by CT images (slice no. 252) with two estimated densities of 2.4 g/cm^3 and 2.9 g/cm^3, respectively. Figure 3c shows the Cs$_2$O concentration map by the EPMA, in a polished section corresponding to slice no. 252. The nondestructive Cs concentration maps are in good agreement with the EPMA map, although some ring artifacts affect the Cs maps. In particular, the Cs$_2$O concentration in the melt by SP-μCT (see blue areas in Fig. 3a) is almost the same as that by the EPMA. The Cs$_2$O concentration of pollucite crystals by SP-μCT (see high concentration areas in Fig. 3b) is also close to that by the EPMA. Owing to these results, we can conclude that this method has high quantitative accuracy if the density of the material is known. Accordingly, the quantitative error in this mapping technique depends largely on the uncertainty of the density.

Figures 3d and 3e show images for comparison of the effective spatial resolution. As mentioned above, the voxel (3-D pixel) size is similar for the EPMA and X-ray CT analyses. The effective spatial resolution of EPMA mapping (electron probe of the X-ray emission area) is considered to be about 6 μm (width) and 3 μm (depth) for the present measurement conditions (Castaing 1960). This 6 μm in-plane resolution of EPMA mapping corresponds to the pixel size (step distance) of the EPMA map in this study. The boundary between the melt and pollucite and that between the melt and quartz are sharp in the EPMA map (Fig. 3e), whereas they are diffuse with width of 3–4 pixels in the SP-μCT map (Fig. 3d). Thus, the effective spatial resolution of SP-μCT mapping is considered to be about 20 μm (3–4 voxels). This spatial resolution is slightly poorer than the 13 μm effective resolution of the SP-μCT system, mentioned previously (Uesugi

et al. 1999; Takano et al. 2001). This difference is probably due to a subtle shift of the voxels (coordinates) between the images above and below the absorption edge, depending on the sample displacement or change in the X-ray path. This spatial resolution of about 20 μm by "nondestructive method" is noteworthy.

Figure 4 shows the difference between Cs$_2$O concentrations measured by SP-μCT and EPMA. Concentrations estimated by SP-μCT (slice no. 252) are compared pixel by pixel with the EMPA map. Most of the data points plot on and around the 1:1 line, although a few points deviate significantly from the line. There are four factors that produce the deviation. (1) The problem of the density estimation is the first factor of the deviation. Figure 4 uses an assumed density of $\rho = 2.65$ g/cm^3, which is the median value of the densities of Cs-bearing melt (2.4 g/cm^3) and pollucite (2.9 g/cm^3). For the first approximation, the assumed density is reasonable because almost all data points ranging from 6 to 30 wt% (larger than the amount dissolved in the melt and smaller than the concentration in pollucite) plot on and around the 1:1 line. These data points include contributions from both melt and pollucite. On the other hand, the data points for concentrations greater than 30 wt% plot far above the line (region A in the figure) because they originate only from pollucite with higher density. (2) The second factor is the artifacts that characteristically appear in X-ray CT images. The deviant points in region B originate mainly in the ring artifact. However, the number of points plotted in region B is very small as shown by the following regression analysis. (3) The third factor is attributed to measurement error by EPMA analysis. The EPMA map also has an error of about 1 wt% and shows larger deviations in some cases, for example, by scratches on the polished surface. (4) The fourth factor is the technical problem of pixel-by-pixel comparison like Figure 4. The complete pixel matching between two images acquired by X-ray CT and EPMA is very difficult and is the principal cause of the deviation. Thus it should be noted that real uncertainties of concentration by SP-μCT is better than that shown in the figure. According to the regression analysis using all data points in Figure 4, the correlation coefficient is 0.91 and the confidence interval of 95.4% probability was estimated as ±2.5 wt%. In this report, we use this confidence interval as the compositional resolution of the 3-D mapping technique although real accuracy ought to be better than that.

3-D concentration mapping and its usefulness

Figure 3f shows the 3-D Cs$_2$O concentration map obtained by stacking 300 slices. The concentration in each slice was corrected using the measured $\Delta\tau_{Cs}$ shown in Figure 2c. In the previous estimation of the element concentration by the subtraction method (Hirano et al. 1989), the published value was used for $\Delta\tau$. However, this value varies depending on the position in the X-ray beam, the energy setting above and below the absorption edge, and other factors. Thus, quantitative reliability in the present study has largely improved.

3-D concentration maps are particularly important for studying material transport in anisotropic materials or partially molten materials. We can derive information on 3-D Cs diffusion from this 3-D concentration map. Of course, some Cs was transported to the inside of the sample by H$_2$O, because Cs was added as water-soluble Cs$_2$CO$_3$ in this study. However, Cs is considered to
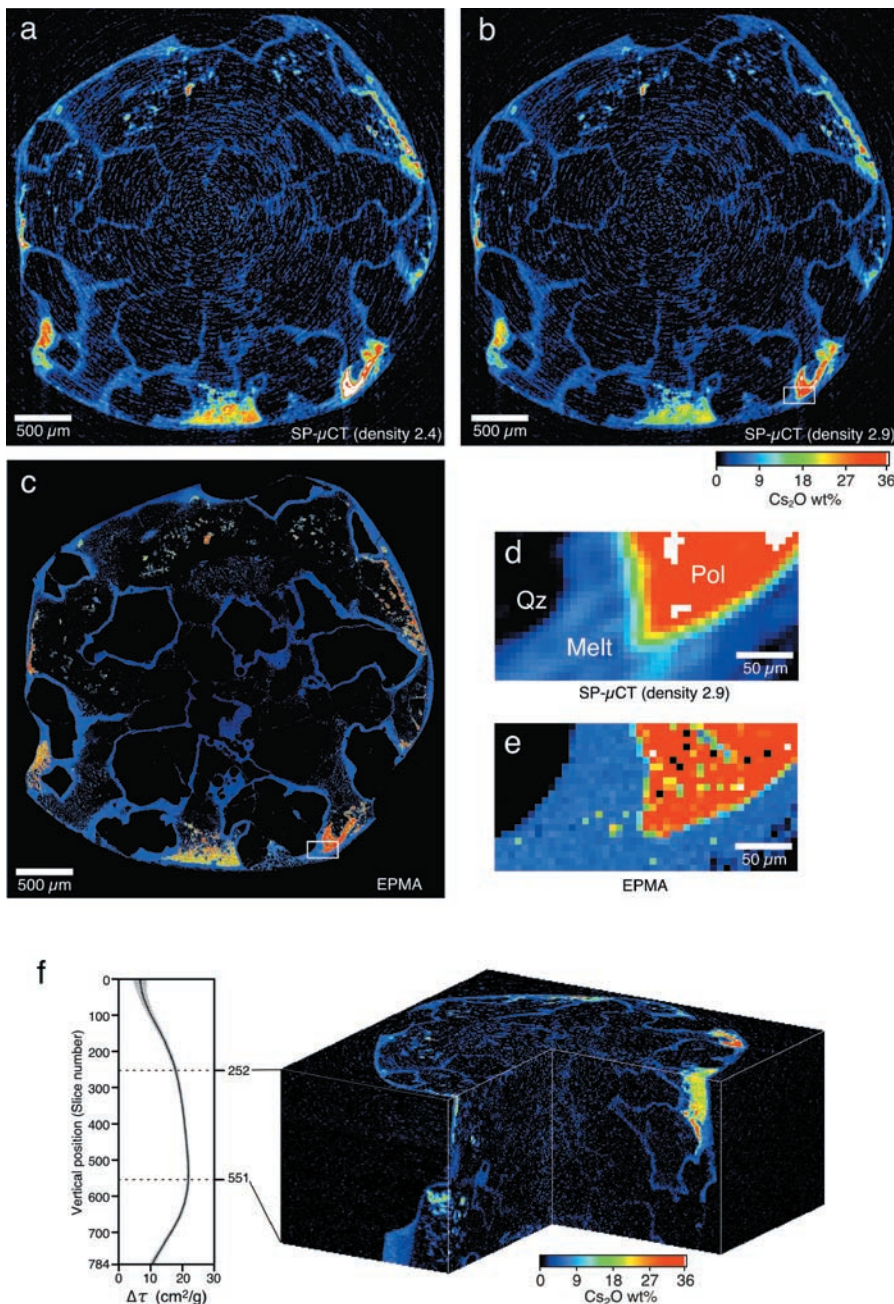
Figure 3. Nondestructive Cs$_2$O concentration maps of slice no. 252 obtained by SP-μCT (650 ×650 voxels). Density is assumed to be **(a)** 2.4 g/cm^3 and **(b)** 2.9 g/cm^3. **(c)** Cs$_2$O concentration map of polished surface obtained by EPMA (650 × 650 pixels). **(d)** Enlarged image of the box region shown in CT image **(b)**: voxel size is 5.83 × 5.83 × 5.83 μm. **(e)** Enlarged image of the box region shown in EPMA image **(c)**: pixel size is 6.0 × 6.0 μm. Mineral names are as follows: Pol = pollucite, Qz = quartz. **(f)** Bird eye's view map of 3-D Cs$_2$O concentration map constructed by stacking 300 tomographic maps (slice nos. 252–551; 650 × 650 × 300 voxels) with density ρ = 2.9 g/cm^3 (corresponding to b). Concentration in each slice was corrected using the measured $\Delta\tau_{Cs,}$ obtained in Figure 2.

have been transported mainly by diffusion in the melt, because the Cs$_2$O concentration decreases toward the center of the sample. Although we have not yet studied the details of the diffusion process (for example, evaluation of the tortuosity of the melt channel), the diffusion coefficient of Cs in partial melt is roughly estimated as on the order of 10^{-10} m^2/s. Such diffusion in partially molten materials has to be studied in three dimensions because the 3-D network structure cannot be investigated precisely in two dimensions (e.g., Ikeda et al. 2000).

3-D network structures of melt or crystals are important and have been the targets of X-ray CT study. For example, Brown et al. (1999) identified the melt network in migmatite (strictly, the network of leucosome in crystallized migmatites) and Philpotts

et al. (1999) discussed 3-D plagioclase chain networks using X-ray CT. They used an ordinary X-ray CT technique, thus, segmentation of leucosome or plagioclase by thresholding was performed based on the difference of LACs. Although they could obtain good binary images of the leucosome or plagioclase, the LACs of melt and minerals are generally very similar in silicate systems and thresholding based on LACs are often difficult. 3-D element-concentration maps are also useful from the point of the thresholding and making quantitative binary images. The 3-D element mapping technique enables us to extract the material of interest by thresholding based on the element concentration. For example, from the results of the 3-D image analysis technique (cluster labeling; Ikeda et al. 2000), 88 vol% of Cs-bearing melt
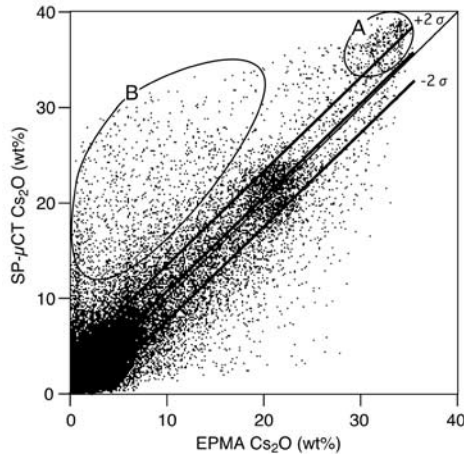
FIGURE 4. Relationship between Cs_2O concentrations measured by EPMA and those by SP-μCT (slice no. 252). The concentrations by SP-μCT were calculated using a density of 2.65 g/cm^3, the median value of melt (2.4) and pollucite (2.9). The corresponding pixels between the images were determined by the appropriate coordinates conversions, scaling, rotation and parallel translation, because the size of pixels and positions of the sample were different in the images. Actual comparison was carried out using the average concentration of $4 \times 4 = 16$ ($\sim 24 \times 24$ μm) pixels as one unit, which corresponds to the spatial resolution of the SP-μCT mapping (20 μm). The central solid line indicates the least-squares fitting in regression analysis and other solid lines indicate the ±2σ (confidence interval of 95.4% probability). Regions A and B are discussed in the text.

regions of 4–6 wt% Cs_2O were connected as the 3-D network. Thus, this 3-D concentration mapping technique is potentially a powerful tool for studying 3-D network structures.

Possibility of diffusion study by the 3-D mapping

The 3-D diffusion study is important and here we discuss the possibility of diffusion studies by this nondestructive 3-D mapping technique. Figure 5a shows theoretical diffusion profiles drawn for various $(Dt)^{1/2}$, where D and t indicate the diffusion coefficient (m^2/s) and time (s), respectively. In the figure, horizontal and vertical intervals of the grid lines correspond to the spatial (~20 μm) and compositional resolution (±2.5 wt%) of the map, respectively. Based on the spatial and compositional resolution, the diffusion profiles of $(Dt)^{1/2}$ ranging from 3×10^{-5} m to 3×10^{-4} m seem to be detected most precisely if the initial concentration of the diffusion source is larger than 30 wt%. Figure 5b shows the relationship between the time scale of geological events and diffusion processes. As described above, diffusion processes plotting in the gray zone, where $(Dt)^{1/2} = 3 \times 10^{-5} - 3 \times 10^{-4}$ m, are the best candidates for the studies. For example, diffusion in silicate melt or glass in experimental samples (fast diffusion in short time scale) is one of the potential targets. Partially molten rocks prepared (quenched) in laboratories are proper samples for investigating diffusion in complicated 3-D network systems. Anisotropic material transport by the combination of diffusion and advection in melt is also an important subject that can be studied by the 3-D mapping technique. Moreover, "nondestructive measurement" enables the in situ diffusion studies. Using the samples having appropriate diffusivity, time-resolved in situ diffusion studies can be performed in the SP-μCT system. In such
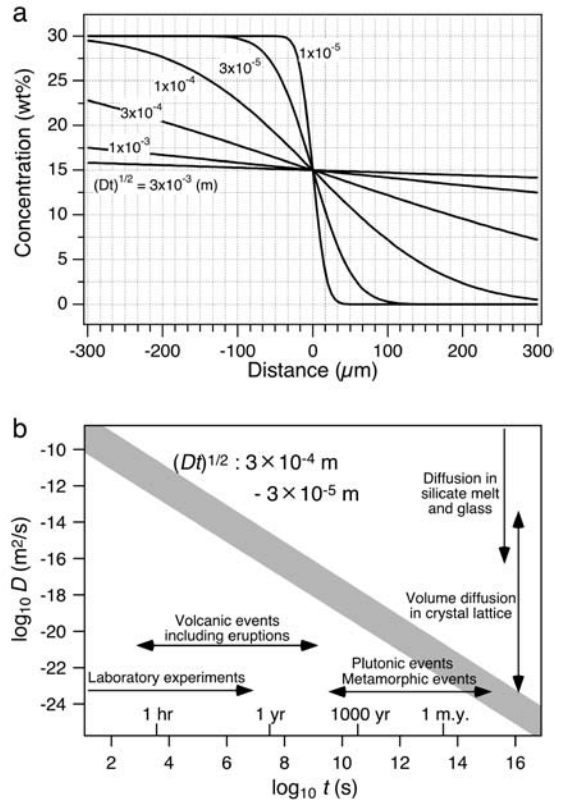

FIGURE 5. (a) Diffusion profiles calculated using the error function assuming an extended source of infinite extent (Crank 1975). The initial concentration was fixed at 30 wt%. Diffusion profiles were drawn for various $(Dt)^{1/2}$. The horizontal and vertical grid lines indicate the spatial resolution and compositional resolution, respectively. **(b)** Relationship between time scale and diffusion coefficients. The gray zone satisfies the condition of $(Dt)^{1/2}$ ranging from 3×10^{-5} to 3×10^{-4} m. The diffusion processes that plot in the gray zone are potential targets of the 3-D mapping technique. The ranges of diffusion processes are based on, for example, Hofmann (1980), Lasaga (1998), and Nakashima (1995).

studies, time-resolution generally corresponds to the acquisition time of one set of the projection images required for the reconstruction, that is, ranges from one to several hours (depending on the target element, its concentration, and the sample diameter). Volume diffusion that occurred in plutonic or metamorphic events (slow diffusion on long time scales) is also the target. Because such slow diffusion cannot be investigated in situ, the traces of anisotropic diffusion left in the natural specimens are candidates for this mapping technique. Therefore, the nondestructive 3-D mapping technique can be used for various 3-D and/or in situ diffusion studies.

Other uses of the nondestructive 3-D mapping technique

Because all elements have absorption edges, this technique can be applied to various samples and elements. As mentioned above, "3-D" compositional information is important in many scientific fields. The "nondestructive" feature of this technique is also important, for example, for obtaining internal-element-concentration maps of precious samples such as cultural assets, which must not be cut. This technique is also useful for curation of extraterrestrial materials, such as precious meteorites
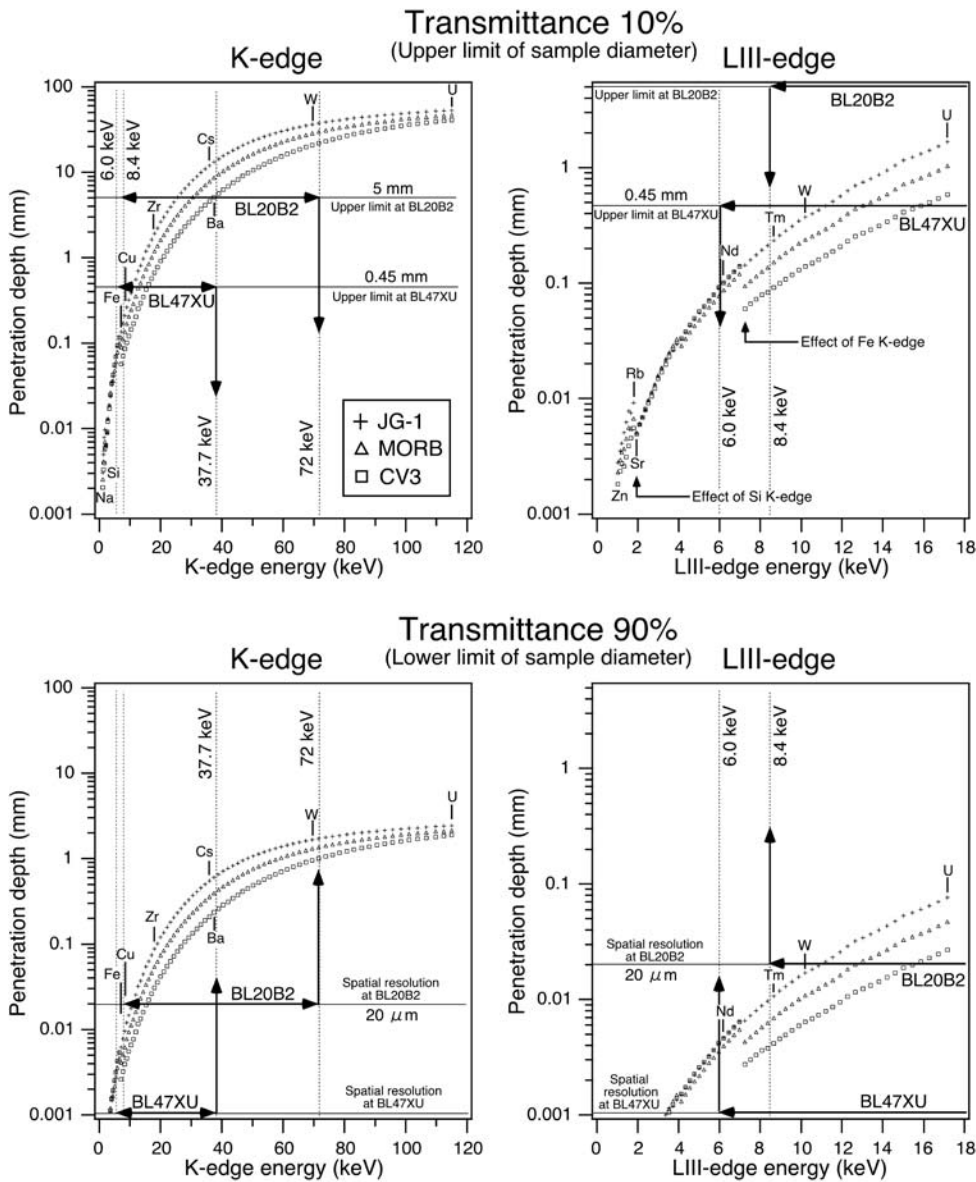
FIGURE 6. Variation of penetration depths of X-ray with the absorption energy for different elements. Data are plotted in order of increasing atomic number. The penetration depths were calculated for a granitic rock, basalt, and a chondritic meteorite. The chemical compositions of Japanese standard granite (granodiorite) JG-1 (Imai et al. 1995), mid-ocean ridge basalt N-MORB (Sun et al. 1979), and Allende meteorite CV3 (Jarosewich 1990) were used. Density was assumed to be 2.7 and 2.9 g/cm^3 for JG-1 and N-MORB, respectively. The density of Allende is 2.92 g/cm^3 (Consolmagno and Britt 1998). Penetration depth of transmittance 10% and 90% correspond to the maximum and minimum sample diameter, respectively. Sample diameter is also restricted by the field of view of the detector (CCD camera), spatial resolution, and usable X-ray energy. These limitations are shown in the figure.

and samples returned by planetary missions. In addition, it is a useful tool for investigation of samples that are easily deformed or damaged by cutting, such as living tissues or fragile, porous materials. So far, our research group has succeeded in obtaining Fe distribution images of Antarctic micrometeorites of less than 100 μm (Tsuchiyama et al. 2001), with a spatial resolution of the order of 1 μm, using the Fe *K*-absorption edge (7.112 keV) at "in-vacuum" type undulator beam line BL47XU (Uesugi et al. 2001) of which X-ray flux density is three orders of magnitude larger than that of BL20B2. The monochromator is an Si (111) double-crystal type. We are now investigating the quantitative accuracy of the Fe concentration estimation in the minerals.

Restriction on sample diameter

Because the X-ray CT technique requires appropriate transmittance of X-ray beams, the sample size (thickness) is first restricted by the transmittance. Secondly, the sample size

is restricted by the field of view of the detector (CCD camera) because the sample is rotated and projection images of the sample should be acquired in all directions without any overflow into the outside of the view (overflow into the direction of the rotation axis has no problem). Thirdly, the sample size is restricted by the usable X-rays energy of the beam lines. Here, we discuss the "sample diameter" as the sample size because a cylindrical shape is the most appropriate one for X-ray CT measurement. If the sample is not cylindrical, the path length of X-ray varies with sample rotation and further consideration is required for this argument.

Figure 6 shows the relationships between energy of the X-ray and penetration depth of which transmittance is 10% and 90%. A transmittance of 10% is empirically the lower limit for obtaining the X-ray CT images sufficient for element concentration measurement. Thus, the penetration depth of 10% transmittance means the maximum diameter (upper limit) of the sample. A

transmittance of 90% is the upper limit for obtaining the X-ray CT images. Thus, the penetration depth of 90% transmittance means the minimum diameter (lower limit) of the sample. Because the energies of X-ray absorption edges are different for different elements, the maximum and minimum sample diameter varies depending upon the target element. These depth data were calculated using the standard compositions of igneous rocks (JG-1 as granitic rocks and N-MORB as basaltic rocks) and a meteorite (CV3) without any other components; thus, the penetration depth decreases if the sample includes a large amount of target heavy elements. According to these calculated data, the upper limit of the sample diameter based on the X-ray penetration is as following examples:

BL20B2 using K-edge (Cu-W are measurable)
  Cu: 80 µm (CV3), 130 µm (MORB), 200 µm (JG-1)
  Cs: 5 mm (CV3), 8 mm (MORB), 12 mm (JG-1)
  W: 20 mm (CV3), 28 mm (MORB), 35 mm (JG-1)
BL20B2 using L^{III}-edge (Tm-U are measurable)
  Tm: 90 µm (CV3), 150 µm (MORB), 220 µm (JG-1)
  U: 600 µm (CV3), 1.0 mm (MORB), 1.7 mm (JG-1)
BL47XU using K-edge (Fe-Ba are measurable)
  Fe: 60 µm (CV3), 90 µm (MORB), 130 µm (JG-1)
  Ba: 5 mm (CV3), 9 mm (MORB), 13 mm (JG-1)
BL47XU using L^{III}-edge (Nd-U are measurable)
  Nd: 100 µm (CV3), 85 µm (MORB), 100 µm (JG-1)
  U: 600 µm (CV3), 1.0 mm (MORB), 1.7 mm (JG-1).

On the other hand, the lower limit of the sample diameter due to the X-ray penetration is, for example, 10 µm, 600 µm and 1.5 mm for Cu, Cs, and W, respectively, when using the JG-1 composition and the K-edge. Using the L^{III}-edge, the lower limit is less than 100 µm even for the heaviest element U.

Besides these limitations due to the X-ray penetration (transmittance), maximum sample diameter is also restricted by the field of view of the detector and by the usable X-ray energy. The widths of the field of view of the detector are 5 mm and 0.45 mm for BL20B2 and BL47XU, respectively. Thus, the actual sample size for Cs measurement at BL20B2 is restricted to 5mm (or less even for the granitic samples). The minimum sample diameter, of course, must be larger than the spatial resolutions of the measurement systems, that is, ~20 µm and ~1 µm for BL20B2 and BL47XU, respectively. In Figure 6, the energy ranges of usable X-ray at BL20B2 and BL47XU are shown. Owing to this energy restriction, the measurable lightest elements are Cu and Fe for BL20B2 and BL47XU, respectively. Although elements heavier than tungsten (W) have K-edges exceeding the usable energy range (<72 keV at BL20B2), such heavy elements have L-absorption edges greater than 12 keV, and therefore can be analyzed by our method. Thus, our 3-D mapping technique is useful in studying various subjects in the earth and materials sciences.

ACKNOWLEDGMENTS

REFERENCES CITED

Bonse, U. and Busch, F. (1996) X-ray computed microtomography (µCT) using synchrotron radiation (SR). Progress in Biophysics and Molecular Biology, 65, 133–169.

Bottinga, Y., Weill, D., and Richet, P. (1982) Density calculations for silicate liquids. I. Revised method for aluminosilicate compositions. Geochimica et Cosmochimica Acta, 46, 909–919.

Brown, M.A., Brown, M., Carlson, W.D., and Denison, C. (1999) Topology of syntectonic melt-flow networks in the deep crust: Interfaces from three-dimensional images of leucosome geometry in migmatites. American Mineralogist, 84, 1793–1818.

Castaing, R. (1960) Electron probe microanalysis. In L. Marton, Ed., Advances in electronics and electron physics, Vol. 13, p. 317–386. Academic Press, New York.

Consolmagno, G.J. and Britt, D.T. (1998) The density and porosity of meteorites from the Vatican collection. Meteoritics & Planetary Science, 33, 1231–1241.

Crank, J. (1975) The mathematics of diffusion, 2nd ed., 414 p. Oxford University Press, Oxford.

Dana, E.S. and Ford, W.E. (1959) A textbook of mineralogy (Modern Asia Edition), 851 p. Charles E Tuttle Company, Tokyo.

Deer, W.A., Howie, R.A., and Zussman, J. (1966) An introduction to the rock-forming minerals, 528 p. Wiley, New York.

Denison, C., Carlson, W.D., and Ketcham, A. (1997) Three-dimensional quantitative textural analysis of metamorphic rocks using high-resolution computed X-ray tomography: Part I. Methods and techniques. Journal of Metamorphic Geology, 15, 29–44.

Flannery, B.P., Deckman, H.W., Roberge, W.G., and D'Amico, K.L. (1987) Three-dimensional X-ray microtomography. Science, 237, 1439–1444.

Goto, S., Takeshita, K., Suzuki, Y., Ohashi, H., Asano, Y., Kimura, H., Matsushita, T., Yagi, N., Isshiki, M., Yamazaki, H., Yoneda, Y., Umetani, K., and Ishikawa, T. (2001) Construction and commissioning of a 215-m long beam line at SPring-8. Nuclear Instruments and Methods in Physics Research A, 467–468, 682–685.

Herman, G.T. (1980) Image reconstruction from projections : the fundamentals of computerized tomography, 316 p. Academic Press, San Francisco.

Hirano, T., Eguchi, S., and Usami, K. (1989) Study of quantitative elemental analysis of monochromatic X-ray CT using synchrotron radiation. Japanese Journal of Applied Physics, 28, 135–139.

Hofmann, A.W. (1980) Diffusion in natural silicate melts: a critical review. In R.B. Hargraves, Ed., Physics of magmatic processes, p. 385–417. Princeton University Press, Princeton.

Hubbell, J.H. and Seltzer, S.M. (1996) Tables of X-Ray Mass Attenuation Coefficients and Mass Energy-Absorption Coefficients from 1 keV to 20 MeV for Elements Z = 1 to 92 and 48 Additional Substances of Dosimetric Interest. (NIST, Physical Laboratory, Physical Reference Data. http://physics.nist.gov/PhysRefData/XrayMassCoef/cover.html),

Ikeda, S., Nakano, T., and Nakashima, Y. (2000) Three-dimensional study on the interconnection and shape of crystals in a graphic granite by X-ray CT and image analysis. Mineralogical Magazine, 64, 945–959.

Imai, N., Terashima, S., Itoh, S., and Ando, A. (1995) 1994 compilation of analytical data for minor and trace elements in seventeen GSJ geochemical reference samples, "Igneous rock series." Geostandards Newsletter, 19, 135–213.

Jarosewich, E. (1990) Chemical-analyses of meteorites—A compilation of stony and iron meteorite analyses. Meteoritics, 25, 323–337.

Johannes, W. and Holtz, F. (1996) Petrogenesis and experimental petrology of granitic rocks, 335 p. Springer-Verlag, Berlin Heidelberg.

Kak, A.C. and Slaney, M. (1988) Principles of computerized tomographic imaging, 329 p. IEEE Press, New York.

Ketcham, A. and Carlson, W.D. (2001) Acquisition, optimization and interpretation of X-ray computed tomographic imagery: application to the geosciences. Computers & Geosciences, 27, 381–400.

Kinney, J., Johnson, Q., Nichols, M.C., Bonse, U., and Nusshardt, R. (1986) Elemental and chemical-state imaging using synchrotron radiation. Applied Optics, 25, 4583–4585.

Lasaga, A.C. (1998) Kinetic theory in the earth sciences, 811 p. Princeton University Press, Princeton.

Nakano, T., Nakashima, Y., Nakamura, K., and Ikeda, S. (2000) Observation and analysis of internal structure of rock using X-ray CT (in Japanese with English abstract). The Journal of the Geological Society of Japan, 106, 363–378.

Nakashima, S. (1995) Diffusivity of ions in pore water as a quantitative basis for rock deformation rate estimates. Tectonophysics, 245, 185–203.

Paktunc, A.D., Lastra, R., and Rivers, M. (2001) Synchrotron-based 3-D mi-

crotomographic imaging of synthetic particles for stereological corrections of liberation measurements and modal analysis (presented at the 40th Annual Conference of Metallurgists of CIM, Toronto, ON., Canada, August, 2001). In J.A. Finch, S.R. Rao, and L. Huang, Eds., Interactions in Mineral Processing, p. 459–472.

Philpotts, A.R., Brustman, C.M., Shi, J., Carlson, W.D., and Denison, C. (1999) Plagioclase-chain networks in slowly cooled basaltic magma. American Mineralogist, 84, 1819–1829.

Roberts, W.L., Papp, G.R. Jr., and Weber, J. (1974) Encyclopedia of minerals, 693 p. Van Nosrand Reinhold Company, New York.

Sun, S.S., Nesbitt, R.W., and Sharaskin, A.Y. (1979) Geochemical characteristics of midocean ridge basalts. Earth and Planetary Science Letters, 44, 119–138.

Suzuki, Y., Usami, K., Sakamoto, K., Kozaka, H., Hirano, T., Shiono, H., and Kohno, H. (1988) X-ray computerized tomography using monochromated synchrotron radiation. Japanese Journal of Applied Physics, 27, L461–L464.

Takano, H., Suzuki, Y., Uesugi, K., Takeuchi, A., and Yagi, N. (2001) PSF measurement of imaging detectors with an X-ray microbeam. Proceedings of SPIE, 4499, 126–133.

Thompson, A.C., Llacer, J., Campbell Finman, L., Hughes, E.B., Otis, J.N., Wilson, S., and Zeman, H.D. (1984) Computed tomography using synchrotron radiation. Nuclear Instruments and Methods in Physics Research, 222, 319–323.

Tsuchiyama, A., Uesugi, K., Nakano, T., Umetani, K., Suzuki, Y., Yagi, N., Tachibana, S., and Kawabata, T. (1999) A study of three-dimensional structures chondrules by an XTM (1999B0112-NOM-np). SPring-8 User Experiment Report on beam line BL20B2: http://www.spring8.or.jp/ENGLISH/user_info/user_ex_repo/

Tsuchiyama, A., Uesugi, K., and Nakano, T. (2000) A study of three-dimensional structures of rocks and minerals using a high-resolution X-ray CT method - primitive materials in the solar system and chondrules (in Japanese with English abstract). Journal of Geography, 109, 845–858.

Tsuchiyama, A., Uesugi, K., Noguchi, T., Yano, H., Nakano, T., and Suzuki, Y. (2001) Three-dimensional microstructures of Antarctic micrometeorites by X-ray computed tomography using synchrotron radiation at SPring-8. Meteoritics & Planetary Science, 36, Suppl. A210.

Uesugi, K., Tsuchiyama, A., Nakano, T., Suzuki, Y., Yagi, N., Umetani, K., and Kohmura, Y. (1999) Development of micro-tomography imaging system for rock and mineral samples (presented at the SPIE Conference on Developments in X-Ray Tomography II, Denver, Colorado, July, 1999). Proceedings of SPIE, 3772, 214–221.

Uesugi, K., Suzuki, Y., Yagi, N., Tsuchiyama, A., and Nakano, T. (2001) Development of high spatial resolution X-ray CT system at BL47XU in SPring-8. Nuclear Instruments and Methods in Physics Research A, 467–468, 853–856.